catalysts

MDPI

Article

Sulfur-Doped TiO_2: Structure and Surface Properties

Sara Cravanzola *, Federico Cesano *, Fulvio Gaziano and Domenica Scarano

Department of Chemistry, NIS (Nanostructured Interfaces and Surfaces) Inter-Departmental Centre and INSTM Centro di Riferimento, University of Torino, Via P. Giuria, 7, 10125 Torino, Italy; fulvio.gaziano@edu.unito.it (F.G.); domenica.scarano@unito.it (D.S.)

* Correspondence: sara.cravanzola@unito.it (S.C.); federico.cesano@unito.it (F.C.); Tel.: +39-011-670-7834 (S.C. & F.C.)

Academic Editors: Vladimiro Dal Santo and Alberto Naldoni
Received: 29 May 2017; Accepted: 11 July 2017; Published: 18 July 2017

Abstract: A comprehensive study on the sulfur doping of TiO_2, by means of H_2S treatment at 673 K, has been performed in order to highlight the role of sulfur in affecting the properties of the system, as compared to the native TiO_2. The focus of this study is to find a relationship among the surface, structure, and morphology properties, by means of a detailed chemical and physical characterization of the samples. In particular, transmission electron microscopy images provide a simple tool to have a direct and immediate evidence of the effects of H_2S action on the TiO_2 particles structure and surface defects. Furthermore, from spectroscopy analyses, the peculiar surface, optical properties, and methylene blue photodegradation test of S-doped TiO_2 samples, as compared to pure TiO_2, have been investigated and explained by the effects caused by the exchange of S species with O species and by the surface defects induced by the strong H_2S treatment.

Keywords: TiO_2; S-doping; sulfidation; HRTEM; XRD; UV-visible; FTIR

1. Introduction

Titanium dioxide (TiO_2) is widely used for photocatalysis. It has attracted considerable attention because of its characteristics, including optical properties, reactivity and chemical stability, as well as its non-toxicity [1,2]. In particular, TiO_2-based photocatalysts have been used for significant applications, such as antibacterial actions [3], medical research [4], drug delivery [5], and self-cleaning fields [6]. Most of all, this material is widely used in the degradation of pollutants in air and water by the decomposition of organic compounds [7,8].

Despite its outstanding photocatalytic properties, TiO_2 is only able to absorb a small range of the UV portion of the solar spectrum [9], because of its relatively high band gap. To solve this problem, the most-used strategy is the engineering and shift of the TiO_2 band gap to the visible light region, in such a way to enhance its photocatalytic activity. In this regard, the surface modification obtained by anchoring selected species, such as MoS_2 or graphene-like systems [10,11], or by the incorporation of metal or non-metal dopants into the TiO_2 structure [12], allows one to harvest the visible spectrum or to increase the reactivity in the UV spectrum. It has been found that metals are able to induce a desired band gap shift, but also induces recombination centers, thus reducing the photocatalysis capability in combination with thermal instability [13].

On the other hand, the incorporation of non-metals, including nitrogen, carbon, sulfur, fluorine, or iodine [14–21], possibly as quantum dots [22], was found to be a more efficient way to lower the band gap of TiO_2, thus obtaining a photocatalyst with higher activity.

Indeed, sulfur-doped TiO_2 has attracted much attention due to the fact that increasing quantities of S can reduce the band gap [23], as well as show a strong absorption in the visible light [24].

Many strategies have been adopted to synthesize S-doped TiO_2 nanocatalysts, from the oxidative annealing of TiS_2, to catalyzed hydrolysis, hydrothermal and solvothermal synthesis, as well as sol-gel and co-precipitation methods [25–28]. In this regard, H_2S can be used as a precursor to obtain an S-doped TiO_2 surface [29].

According to some authors, the mechanism of H_2S adsorption on the TiO_2 surface is explained with dissociative pathways, causing S to fill the O vacancies to obtain S-doped surfaces [29].

However, the integration mechanism of S in TiO_2, from a structural point of view, is still under debate, being to a great extent affected by the synthesis conditions. It has been reported that sulfur could be adsorbed predominantly in the form of SO_4^{2-} species at the surface of TiO_2 nanoparticles [30], or could be embedded within the TiO_2 lattice, thus creating S-Ti-O bonds [31].

Therefore, to better understand and describe the properties and then the possible applications of the so-obtained S-doped TiO_2, it is fundamental to investigate the nature of the H_2S interaction with the TiO_2 surface.

Moreover, a further aspect to take into account is the role of H_2S as a reactant in catalytic hydro-treatment and Claus reactions [32,33]. It is noteworthy that, nowadays, the emission limits of SO_x are becoming very rigorous, because air pollution has become a serious global problem. Oil and gas extraction sites are one of the main sources of H_2S emissions, and they are usually removed by means of the well-known Claus process. The reaction occurs via dissociative adsorption of H_2S on a metal oxide [34], mainly on Al_2O_3 but also on TiO_2, used as catalyst.

In both processes, H_2S was found to modify the surface properties of the metal oxide support catalyst. According to the literature, many theoretical studies concerning H_2S reaction and adsorption on TiO_2 are known, particularly those on anatase and rutile phases [35–39].

To our knowledge, only a few experimental studies have focused on the effects originated by H_2S dosage on TiO_2 surface, concerning the relationship among surface, structure, and morphology properties. Our study aims to contribute to these themes, as it reports a quite extensive chemical and physical characterization of the surface properties of S-doped TiO_2, obtained after H_2S treatment. The samples are investigated by X-ray diffraction (XRD), and high resolution transmission electron microscopy (HRTEM), in addition to Raman, Fourier Transform-Infrared (FTIR) and UV-visible (UV-Vis) spectroscopies. The obtained results are compared to those of pure TiO_2.

2. Results and Discussion

2.1. Structure and Morphology by XRD, Raman, and HRTEM Analyses

2.1.1. XRD Analysis

The XRD patterns of TiO_2 before and after H_2S dosage at 673 K for 1 h are shown in Figure 1 (black and red lines, respectively), together with the typical crystalline features of anatase (PDF card # 21-1272) and rutile (PDF card # 21-1276) phases, as highlighted by blue and green lines (anatase and rutile, respectively).

From the pattern of TiO_2 after the sulfidation procedure, no considerable modifications of the peculiar peaks of anatase and rutile are observed, thus remarking that the amount of S species inside the S-doped TiO_2 does not affect the lattice under the adopted preparation conditions. We shall return to this point by analyzing the amount of sulfur via elemental analysis, as illustrated in Figure S1.

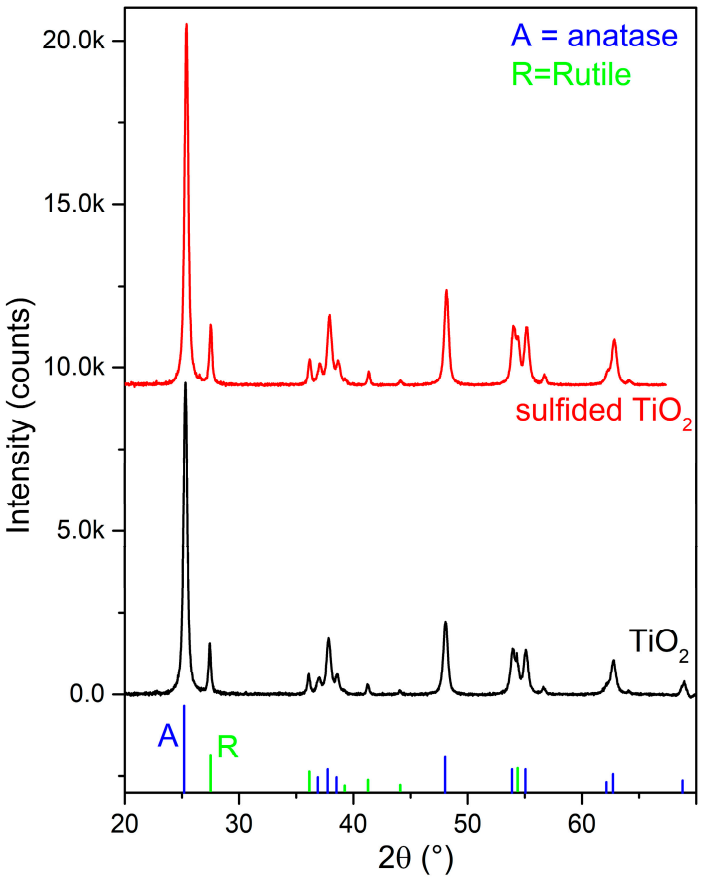

Figure 1. XRD patterns of TiO_2 (black line) and S-doped TiO_2 (red line). Anatase (PDF card # 21-1272) and rutile (PDF card # 21-1276) phases (blue and green lines, respectively) are shown for comparison.

2.1.2. Raman Spectroscopy

Figure 2 shows the Raman spectrum of S-doped TiO_2 compared with pure TiO_2, used as a reference material, both recorded with a 514 nm laser line.

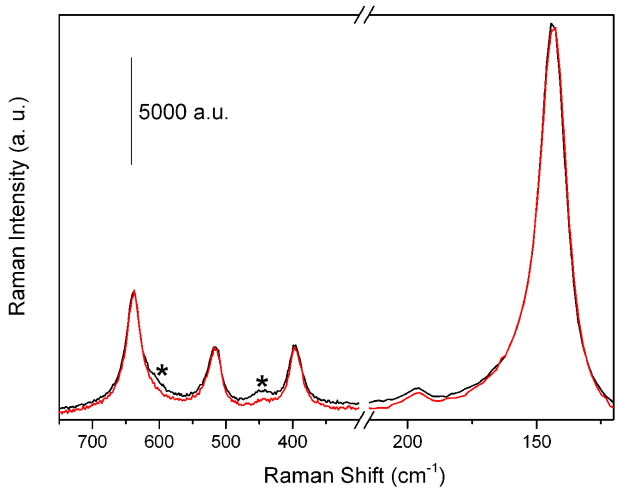

Figure 2. Raman spectra of TiO_2 and S-doped TiO_2 (black and red lines, respectively). Raman fingerprints of rutile are marked by asterisks.

In detail, concerning the spectrum of pure TiO_2 (black curve), the four bands at 144, 396, 514, and 636 cm^{-1} are ascribed to the E_g, B_{1g}, A_{1g}, E_g Raman active modes, respectively, of the anatase phase, as described in the literature [10,18,40]. Furthermore, the shoulder at 608 cm^{-1} and the small peak at 444 cm^{-1} (labelled by asterisks) are due to the A_{1g} and E_g modes of the rutile phase [40]. As for the S-doped TiO_2 sample, as obtained after the sulfidation step (red curve), the typical Raman fingerprints of TiO_2 are still present, even if a clear explanation of the erosion of the weak modes labelled by asterisks remains unclear [29,35].

2.1.3. Surface Area and HRTEM Analysis

Figure 3a,b depict HRTEM images of nanoparticles of ~15–50 nm in size, exposing lattice fringes spaced ~0.32 nm or 0.35 nm, corresponding to (110) and (101) planes of rutile and anatase, respectively, as confirmed by the fast Fourier transform (FFT) investigations (insets of Figure 3b,d).

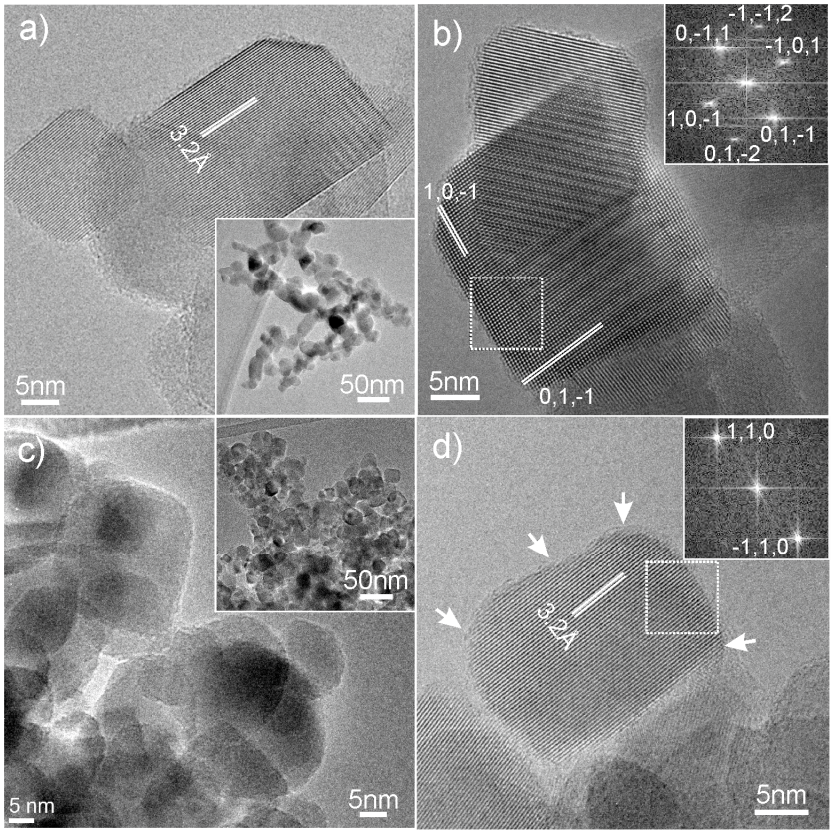

Figure 3. TEM images of TiO_2 (**a**,**b**) and S-doped TiO_2 (**c**,**d**). In the insets of (**a**,**c**) low resolution images of TiO_2 and S-doped TiO_2 are shown, while in the insets of (**b**,**d**) two selected regions are Fast Fourier Transform (FFT) imaged.

In particular, rutile (Figure 3a) and anatase (which reveals its diffraction pattern from [111] zone axis) nanoparticles (Figure 3b), which have a well-defined structure and shape, show extended faces with highly regular terminations, together with sharp corners and edges. Conversely, in Figure 3c,d, S-doped TiO_2 particles with rounded shapes are shown, as highlighted by the white arrows. From Figure 3d, it can be observed that the borders of the particle appear to be completely indented, with corners and edges sensitively smoothed, which is caused by the formation of local defective regions at the atomic level. The explanation of this phenomenon could be plausibly ascribed to the action of H_2S, whose strong acidic character could lead to remarkably defective surfaces of TiO_2 particles.

For a deeper understanding of the effects of H_2S treatment, the TiO_2 and S-doped TiO_2 samples were investigated by low resolution TEM (insets in Figure 3a,c, respectively). From the comparison of the related particle size distributions shown in Figure S2 (Supplementary Materials), a slight increment of particle dimensions for S-doped TiO_2 is detectable, as confirmed by the mean crystal sizes provided by the anatase (101) and rutile (110) XRD peak broadenings (Scherrer's equation) shown in Table S1 (Supplementary Materials).

Moreover, the slight decreasing of the specific surface area (38 m^2/g) of S-doped TiO_2 observed, as compared with TiO_2 (50 m^2/g), in addition to the slight increasing of the particle size in the case of S-doped TiO_2 samples, can be explained by the moderate sintering effect due to annealing treatment conditions occurring at 673 K under an H_2S atmosphere.

Furthermore, the impressive action of H_2S on the nature of TiO_2 particles has been also confirmed by FTIR investigation (*vide infra*).

2.2. Surface Properties by FTIR and UV-Vis Spectroscopies

2.2.1. FTIR Spectroscopy

FTIR spectra collected at 100 K at decreasing CO coverage on TiO_2 were compared to a similar sequence on the S-doped TiO_2 sample (Figure 4a,b). The spectra were acquired by increasing an initial CO dose (70 Torr) to reach equilibrium conditions, i.e., the maximum CO coverage, after which the system was progressively outgassed up to the complete removal of the adsorbed CO molecules.

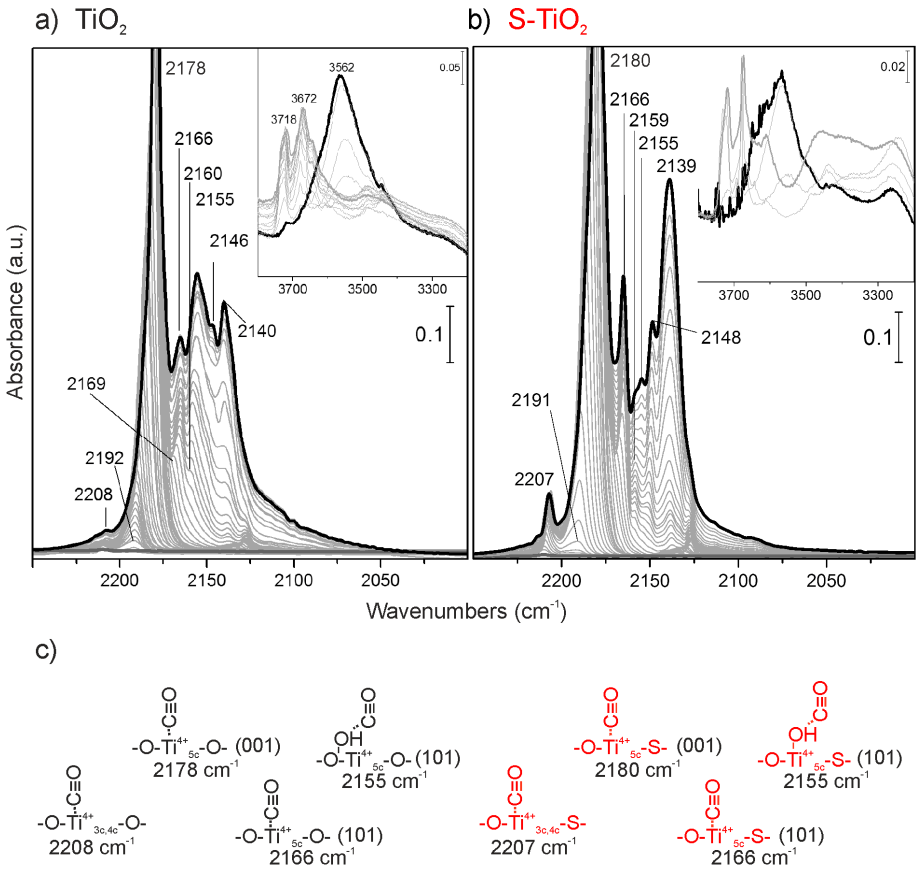

Figure 4. FTIR spectra of CO adsorbed at 100 K on (**a**) TiO_2 and (**b**) S-doped TiO_2 at decreasing coverages (black bold line, maximum coverage: p_{CO} = 70 Torr, grey bold line, minimum coverage: $p_{CO} \rightarrow 0$); (**c**) scheme modelling of Ti sites on two different faces interacting with CO molecules and the frequency values of the corresponding bands at maximum coverage (black bold line).

TiO_2 spectra show the typical features due to the adsorption of CO on the different Ti sites on activated TiO_2 surfaces, as discussed in the literature (Figure 4a) [41–43].

As can be seen from Figure 4a, the intense main peak observed at 2179 cm^{-1} can be explained by the building up of lateral interactions among an array of parallel CO oscillators, adsorbed on Ti^{4+} sites on flat (101) surfaces [41], while that at 2155 cm^{-1} is due to CO molecules interacting by hydrogen bonds with residual OH groups. The main band, in the 2178 cm^{-1}–2192 cm^{-1} range (Figure 4a), undergoes a frequency shift upon decreasing CO pressure, due to the changing of the lateral interactions between CO oscillators on the TiO_2 surface [43,44]. Notice that a higher frequency shift is indicative of a highly regular and extended face.

Coming back to OH groups, which remain on the surface despite the activation treatment at 673 K, their presence is confirmed by the stretching modes observed at 3718 cm^{-1} and 3672 cm^{-1} (inset of Figure 4a). These features are shifted to lower frequency as a consequence of CO adsorption, thus giving rise to a broad and more intense feature centered at 3562 cm^{-1}. Notice that the spectral features of the OH groups are then completely restored at a lower CO pressure together with the progressively disappearing and shifting of the 2155 cm^{-1} band to 2160 cm^{-1}. These two events indicate that the complete and reversible CO desorption from OH groups is occurring [42,45].

The sharp band at 2140 cm^{-1} is easily associated to physically adsorbed CO, which forms a multi-layer surface when the liquid nitrogen temperature brings CO to a "liquid-like" state [46]. On the other hand, the band at 2146 cm^{-1} that, by decreasing CO coverage, gradually shifts upward and merges with the 2155 cm^{-1} band, is due to the CO species on rutile facelets present in TiO_2 P25 [41].

The weak feature at 2166 cm^{-1} was assigned to CO adsorbed on Ti Lewis centers on (001) surfaces, where Ti sites along Ti-O rows are strongly bound to two oxygens, which cause a screened electrostatic potential at these Ti sites, as concluded by Mino et al. [47] in a combined FTIR/Density Functional Theory (DFT) study on the CO adsorption on anatase (001) and (101) facets.

The weak band at 2208 cm^{-1} was assigned to CO adsorbed on highly acid Ti Lewis sites located on defective situations such as edges, steps, and corners, thus exhibiting very low coordination [41].

After H_2S dosage (Figure 3b), some modifications can be highlighted. In particular, a slightly wider Full Width at Half Maximum (FWHM) for the main feature at 2180 cm^{-1} is observed due to a more disordered system, caused by the presence of S species interrupting the regularity of the extended faces.

Notice that the 2180 cm^{-1}–2191 cm^{-1} main band for S-doped TiO_2 (Figure 4b) undergoes a quite similar frequency shift upon decreasing CO pressure, as compared to pure TiO_2 (Figure 4a).

The 2166 cm^{-1} band, previously assigned to Ti Lewis centers on flat (001) faces and strongly bound to O anions, presents an increased intensity and can be ascribed to a reduced screening electrostatic potential due to the O → S exchange. In fact, the presence of sulfur could cause an increased acidity followed by the observed increased intensity (Figure 4b). Conversely, the reduced intensity of the 2160–2155 cm^{-1} envelope can be explained by the weaker interaction of CO molecules with the residual OH groups (Figure 4b).

Moreover, notice that the band at 2207 cm^{-1}, ascribed to CO on highly cus (coordinatively unsaturated) Ti sites on S-doped TiO_2 [41], shows higher intensity with respect to pure TiO_2 and is the last one to disappear by outgassing. It can be hypothesized that the larger S atoms replace the smaller O ones, thus favoring the formation of defects such as edges, steps, and corners.

These results can be confirmed by the wide band observed in the 3400–3200 cm^{-1} region, before CO dosage, due to the formation of surface H_2O as a consequence of oxygen-sulfur exchange (inset of Figure 4b), as explained in the next paragraph.

On the basis of studies concerning the dissociative adsorption of H_2S on TiO_2 [48], it was found that above a temperature of 593 K, the Ti–SH bond is still strong, being –SH irreversibly adsorbed on the surface of TiO_2. However, by increasing the temperature, S-H bonds become weaker and finally break. H moves to a neighboring O, forming –OH groups. Finally H_2O is formed at the surface and S moves to oxygen vacancy positions [29].

Moreover, besides the dissociative adsorption, H_2S molecules can also interact with surface –OH groups (bonded to Ti^{4+}) to give rise to hydrogen bonds.

2.2.2. UV-Vis Spectroscopy

The UV-Vis spectrum of S-doped TiO_2 (red curve) as compared to pure TiO_2 (black curve), is shown in Figure 5. From this, a wide shift of the absorption edge for the S-doped TiO_2 sample towards higher wavelengths (lower energies) is clearly detectable, together with an additional wide absorption centered at around 390 nm.

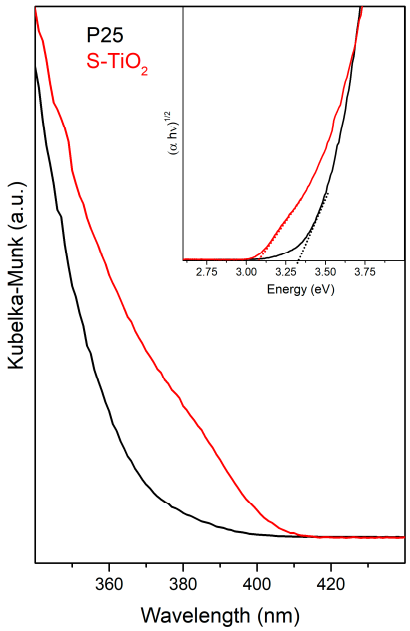

Figure 5. UV-Vis spectra of S-doped TiO_2 (red curve) and pure TiO_2 (black curve) used as a reference material. The Tauc plot of both samples is shown in the inset. An example of a Tauc Plot is reported in ref. [49].

In particular, the band gap shift is emphasized by the Tauc plot (see inset in Figure 5), where the intercepts with the abscissa axis of the extrapolation of the linear part of the curves clearly highlight a red shift of the absorption edge for S-doped TiO_2 (see black and red dotted lines for TiO_2 and S-doped TiO_2, respectively).

In general, this energy red-shift is associated with a change of TiO_2 electronic structure, after the treatment with H_2S, which causes the S $\rightarrow$ O exchange at the surface of TiO_2 [50,51]. Taking into consideration this aspect, it is well known that the formation of doping states involves additional electronic levels that can be formed between the valence (VB) and the conduction (CB) bands, thus reducing the electron transition energy [21,52]. Along this line, the features in the UV-visible range can be ascribed to the presence of additional electronic states above the valence band edge of pure TiO_2, due to S species, as well supported by XPS measurements [52,53]. These states can be attributed to sulfur 3p atomic orbitals mixing with the VB of TiO_2. In addition, another plausible mechanism to explain the observed absorption shift could also involve O vacancies caused by the thermal treatment at 673 K under vacuum conditions [54].

The S-doped TiO_2 sample was testedfor the photodegradation of methylene blue (MB) in water solution under solar light irradiation as compared to the TiO_2 P25 benchmark (Figure S4, Supplementary Materials). In this figure, the MB C/C_0 vs. time plots of S-TiO_2 and of the TiO_2 P25 are shown. Although the MB photodegradation of S-doped TiO_2 is definitely high, under solar light irradiation its photocatalytic activity is lower than that of pure TiO_2 P25. We think that the explanation

for this lower photocatalytic performance in the degradation of MB is the balance of two opposite effects. The first one, associated with the sulfur doping which allows the solar light harvesting, is beneficial. However, the defective surface, as a result of the heavy H_2S treatment, has a strong, definitely detrimental effect in the charge separation efficiency. It is safely concluded that, upon the adopted H_2S conditions (673 K, vacuum), the non-reversible surface modification does not help to increase the photocatalytic efficiency with respect to the TiO_2 P25 powder used as a starting material.

3. Materials and Methods

TiO_2 (P25, Evonik), in pellet form, was activated at 673 K for 30 min under dynamic vacuum, then oxidized in an oxygen (40 Torr) atmosphere at the same temperature for 30 min, twice. By keeping the temperature at 673 K, the obtained sample was sulfided in an H_2S atmosphere (30 Torr) for 1 h, twice, and then outgassed. The sample was further sulfided following the same method.

FTIR spectra of CO adsorbed at 100 K on TiO_2 and S-doped TiO_2 at decreasing coverages were obtained in an IR cell designed for liquid nitrogen flowing, and were recorded by means of a Bruker IFS-28 spectrometer, equipped with a Mercury Cadmium Telluride (MCT) cryogenic detector, with a resolution of 4 cm^{-1} (64 interferograms were averaged for each spectrum). The spectra were acquired in the 4000–400 cm^{-1} interval, where the fundamental vibration modes are observed.

Raman spectra were recorded using a Renishaw Raman InVia Reflex spectrophotometer equipped with an Ar+ laser emitting at 514 nm, using both static and rotating configurations.

UV-Vis measurements were collected by using a UV-Vis-NIR spectrophotometer (Varian Cary 5000, equipped with a reflectance sphere. Due to their strong optical absorption, the samples were diluted in $BaSO_4$ powder.

X-ray diffraction patterns were collected by means of a diffractometer (PANalytical PW3050/60 X'Pert PRO MPD) with a Ni-filtered Cu anode, working with a reflectance Bragg-Brentano geometry, by using the spinner mode. The mean crystal sizes were calculated from XRD measurements by Scherrer's equation: $L = K\lambda/\beta \cos\theta$ (λ is the X-ray wavelength, β is the full width at half maximum (FWHM) of the diffraction line corrected by the instrumental broadening, θ is the diffraction angle, and K is a constant assumed to be 0.9). Peak fitting of XRD patterns was adopted, using the Pseudo-Voigt function of anatase (101) and rutile (110) XRD peaks.

High resolution transmission electron microscopy images were acquired with a JEOL 3010-UHR instrument operating at 300 kV, equipped with a 2 k $\times$ 2 k pixels Gatan US1000 CCD camera.

N_2 adsorption-desorption experiments were carried out at 77 K (Micromeritics ASAP 2020 instrument) to determine the Brunauer-Emmett-Teller (BET) surface area. The surface area of the samples was determined after outgassing at RT, overnight.

For the photodegradation test, the same quantities of S-doped TiO_2 and TiO_2 powder (used as a reference) were dispersed in aliquots of a methylene blue (MB) water solution 12.5 mg/L and kept in the dark for 1 h at RT. After exposure, for increasing times, to a solar lamp (SOL2/500S lamp, Honle UV technology, Munchen, Germany) ranging from ultraviolet to infrared radiation (295–3000 nm), the dispersions were centrifuged for 30 min at 10,000 rpm. Photocatalytic degradation of MB was investigated by means of UV-Vis spectroscopy in the transmission mode. The integrated intensity of the adsorbed MB manifestations (C) was used to obtain C/C_0 vs. time plots, where C_0 is the concentration at the initial intensity before illumination (Figure S4).

4. Conclusions

In this work, S-doped TiO_2 samples were synthesized by means of H_2S treatment at 673 K. From several ex situ investigations, including XRD, Raman spectroscopy, and HRTEM, the structure and morphology of samples were obtained. In particular, even if XRD and Raman analyses, due to detection limits, did not give sensitive information concerning the effects of H_2S dosage on TiO_2, HRTEM images showed remarkable changes of TiO_2 particle shapes as a consequence of H_2S, which causes strong erosion of the faces, corners, and edges of the nanoparticles. This impressive action was

also confirmed by FTIR spectra, where remarkable differences in the relative intensity of all peaks in S-doped TiO_2, when compared to pure TiO_2, were observed. Moreover, the changes in the OH groups range can be ascribed to oxygen-sulfur exchange phenomena, explained with the dissociative adsorption of H_2S on TiO_2.

Finally, UV-Vis spectroscopy demonstrated how also the electronic structure of TiO_2 can be deeply modified by H_2S. The red shift of the S-doped TiO_2 absorption edge can be explained with additional extrinsic electronic levels introduced by the sulfur doping. This affected the optical properties of TiO_2, whose absorption edge was extended to the visible-light region.

From all these considerations, it can be safety concluded that H_2S treatment of TiO_2, to achieve an S-doped TiO_2 material, has a deep and strong effect on TiO_2, such as on the morphological, surface, electronic, and optical properties. However, the photocatalysis efficiency of TiO_2 in the degradation of methylene blue is not improved by the H_2S treatment at the adopted conditions, due to the strongly defective surface of S-doped TiO_2 which decreases the charge separation efficiency.

Supplementary Materials: The following are available online at www.mdpi.com/2073-4344/7/7/214/s1, Figure S1: EDAX spectrum of TiO_2/H_2S, Figure S2: Particle size distributions (PSDs) of TiO_2 P25 (left panel) and of S-TiO_2 (right panel), Figure S3: Time dependence of C/C_0 upon solar light exposure of S-TiO_2 (red line) as compared to the TiO_2 P25 (black dotted line), for photodegradation of methylene blue, Figure S4: FTIR spectra, recorded before CO dosage, of TiO_2 (black curve) and TiO_2/H_2S (red curve), Table S1: Mean crystal sizes of anatase and rutile nanoparticles in TiO_2 P25 and S-TiO_2 samples, as obtained from XRD peak broadening (black and red patters in Figure 1).

Acknowledgments: This work was supported by MIUR (Ministero dell'Istruzione, dell'Università e della Ricerca), INSTM Consorzio and NIS (Nanostructured Interfaces and Surfaces) Inter-Departmental Centre of University of Torino. The authors thank the vibrational Raman spectroscopy laboratory of Chemistry Department and in particular Alessandro Damin, for the precious support in Raman experiments.

Author Contributions: Sara Cravanzola, Federico Cesano and Fulvio Gaziano conceived, designed and performed the experiments and characterizations, analyzing the data; Sara Cravanzola, Federico Cesano and Domenica Scarano wrote the paper. All authors read and approved the paper.

Conflicts of Interest: The authors declare no conflict of interest.

References

1. Nakata, K.; Fujishima, A. TiO_2 photocatalysis: Design and applications. *J. Photochem. Photobiol. C* **2012**, *13*, 169–189. [CrossRef]
2. Schneider, J.; Matsuoka, M.; Takeuchi, M.; Zhang, J.; Horiuchi, Y.; Anpo, M.; Bahnemann, D.W. Understanding TiO_2 photocatalysis: Mechanisms and materials. *Chem. Rev.* **2014**, *114*, 9919–9986. [CrossRef] [PubMed]
3. Kubacka, A.; Diez, M.S.; Rojo, D.; Bargiela, R.; Ciordia, S.; Zapico, I.; Albar, J.P.; Barbas, C.; Martins dos Santos, V.A.P.; Fernández-García, M.; et al. Understanding the antimicrobial mechanism of TiO_2-based nanocomposite films in a pathogenic bacterium. *Sci. Rep.* **2014**, *4*, 1–9. [CrossRef] [PubMed]
4. Yin, Z.F.; Wu, L.; Yang, H.G.; Su, Y.H. Recent progress in biomedical applications of titanium dioxide. *Phys. Chem. Chem. Phys.* **2013**, *15*, 4844–4858. [CrossRef] [PubMed]
5. Song, Y.-Y.; Schmidt-Stein, F.; Baue, S.; Schmuki, P. Amphiphilic TiO_2 nanotube arrays: An actively controllable drug delivery system. *J. Am. Chem. Soc.* **2009**, *131*, 4230–4232. [CrossRef] [PubMed]
6. Banerjee, S.; Dionysioub, D.D.; Pillai, S.C. Self-cleaning applications of TiO_2 by photo-induced hydrophilicity and photocatalysis. *Appl. Catal. B* **2015**, *176–177*, 396–428. [CrossRef]
7. Ao, C.H.; Lee, S.C. Indoor air purification by photocatalyst TiO_2 immobilized on an activated carbon filter installed in an air cleaner. *Chem. Eng. Sci.* **2005**, *60*, 103–109. [CrossRef]
8. Cesano, F.; Pellerej, D.; Scarano, D.; Ricchiardi, G.; Zecchina, A. Radially organized pillars of TiO_2 nanoparticles: Synthesis, characterization and photocatalytic tests. *J. Photochem. Photob. A Chem.* **2012**, *242*, 51–58. [CrossRef]
9. Chatterjee, D.; Mahata, A. Visible light induced photo-degradation of organic pollutants on dye adsorbed TiO_2 surface. *J. Photochem. Photobiol. A* **2002**, *153*, 199–204. [CrossRef]

10. Cravanzola, S.; Cesano, F.; Gaziano, F.; Scarano, D. Carbon domains on MoS_2/TiO_2 system via catalytic acetylene oligomerization: Synthesis, structure and surface properties. *Front. Chem.* **2017**, submitted.
11. Cravanzola, S.; Muscuso, L.; Cesano, F.; Agostini, G.; Damin, A.; Scarano, D.; Zecchina, A. MoS_2 nanoparticles decorating titanate-nanotube surfaces: Combined microscopy, spectroscopy, and catalytic studies. *Langmuir* **2015**, *31*, 5469–5478. [CrossRef] [PubMed]
12. Uddin, M.J.; Cesano, F.; Bertarione, S.; Bonino, F.; Bordiga, S.; Scarano, D.; Zecchina, A. Tailoring the activity of Ti-based photocatalysts by playing with surface morphology and silver doping. *J. Photochem. Photob. A Chem.* **2008**, *196*, 165–173. [CrossRef]
13. Asahi, R.; Morikawa, T.; Ohwaki, T.; Aoki, K.; Taga, Y. Visible-light photocatalysis in nitrogen-doped titanium oxides. *Science* **2001**, *293*, 269–271. [CrossRef] [PubMed]
14. Hong, X.; Wang, Z.; Cai, W.; Lu, F.; Zhang, J.; Yang, Y.; Ma, N.; Liu, Y. Visible-light-activated nanoparticle photocatalyst of iodine-doped titanium dioxide. *Chem. Mater.* **2005**, *17*, 1548–1552. [CrossRef]
15. Dozzi, M.V.; D'Andrea, C.; Ohtani, B.; Valentini, G.; Selli, E. Fluorine-doped TiO_2 materials: Photocatalytic activity vs. time-resolved photoluminescence. *J. Phys. Chem. C* **2013**, *117*, 25586–25595. [CrossRef]
16. Cravanzola, S.; Jain, S.M.; Cesano, F.; Damin, A.; Scarano, D. Development of a multifunctional TiO_2/MWCNT hybrid composite grafted on a stainless steel grating. *RSC Adv.* **2015**, *5*, 103255–103264. [CrossRef]
17. Ansari, S.A.; Khan, M.M.; Ansaric, M.O.; Cho, M.H. Nitrogen-doped titanium dioxide (N-doped TiO_2) for visible light photocatalysis. *New J. Chem.* **2016**, *40*, 3000–3009. [CrossRef]
18. Cesano, F.; Bertarione, S.; Damin, A.; Agostini, G.; Usseglio, S.; Vitillo, J.G.; Lamberti, C.; Spoto, G.; Scarano, D.; Zecchina, A. Oriented TiO_2 nanostructured pillar arrays: Synthesis and characterization. *Adv. Mater.* **2008**, *20*, 3342–3348. [CrossRef]
19. Ramandi, S.; Entezari, M.H.; Ghows, N. Sono-synthesis of solar light responsive S–N–C–tri doped TiO_2 photo-catalyst under optimized conditions for degradation and mineralization of diclofenac. *Ultrason. Sonochem.* **2017**, *38*, 234–245. [CrossRef] [PubMed]
20. Brindha, A.; Sivakumar, T. Visible active N, S co-doped TiO_2/graphene photocatalysts for the degradation of hazardous dyes. *J. Photochem. Photobiol. A* **2017**, *340*, 146–156. [CrossRef]
21. Cesano, F.; Agostini, G.; Scarano, D. Nanocrystalline TiO_2 micropillar arrays grafted on conductive glass supports: Microscopic and spectroscopic studies. *Thin Solid Films* **2015**, *590*, 200–206. [CrossRef]
22. Uddin, M.J.; Daramola, D.E.; Velasquez, E.; Dickens, T.J.; Yan, J.; Hammel, E.; Cesano, F.; Okoli, O.I. A high efficiency 3D photovoltaic microwire with carbon nanotubes (CNT)-quantum dot (QD) hybrid interface. *PSS RRL* **2014**, *8*, 898–903. [CrossRef]
23. Hui, F.; Bu, C. DFT description on electronic structure and optical absorption properties of anionic S-doped anatase TiO_2. *J. Phys. Chem. B* **2006**, *110*, 17866–17871.
24. Smith, M.F.; Setwong, K.; Tongpool, R.; Onkaw, D.; Naphattalung, S.; Limpijumnong, S.; Rujirawat, S. Identification of bulk and surface sulfur impurities in TiO_2 by synchrotron X-ray absorption near edge structure. *Appl. Phys. Lett.* **2007**, *91*, 142107. [CrossRef]
25. Liu, G.; Sun, C.; Smith, S.C.; Wang, L.; Lu, G.Q.; Cheng, H.-M. Sulfur doped anatase TiO_2 single crystals with a high percentage of {0 0 1} facets. *J. Colloid Interface Sci.* **2010**, *349*, 477–483. [CrossRef] [PubMed]
26. Nam, S.-H.; Kim, T.K.; Boo, J.-H. Physical property and photo-catalytic activity of sulfur doped TiO_2 catalysts responding to visible light. *Catal. Today* **2012**, *185*, 259–262. [CrossRef]
27. Yang, G.; Yan, Z.; Xiao, T. Low-temperature solvothermal synthesis of visible-light-responsive S-doped TiO_2 nanocrystal. *Appl. Surf. Sci.* **2012**, *258*, 4016–4022. [CrossRef]
28. Dozzi, M.V.; Livraghi, S.; Giamello, E.; Selli, E. Photocatalytic activity of S- and F-doped TiO_2 in formic acid mineralization. *Photochem. Photobiol. Sci.* **2011**, *10*, 343–349. [CrossRef] [PubMed]
29. Chen, Y.; Jiang, Y.; Li, W.; Jin, R.; Tang, S.; Hu, W. Adsorption and interaction of H_2S/SO_2 on TiO_2. *Catal. Today* **1999**, *50*, 39–47.
30. Wei, F.; Ni, L.; Cui, P. Preparation and characterization of N–S-codoped TiO_2 photocatalyst and its photocatalytic activity. *J. Hazard. Mater.* **2008**, *156*, 135–140. [CrossRef] [PubMed]
31. Li, H.; Zhang, X.; Huo, Y.; Zhu, J. Supercritical preparation of a highly active S-doped TiO_2 photocatalyst for methylene blue mineralization. *Environ. Sci. Technol.* **2007**, *41*, 4410–4414. [CrossRef] [PubMed]
32. Travert, A.; Maugé, F. IR study of hydrotreating catalysts in working conditions: Comparison of the acidity present on the sulfided phase and on the alumina support. *Stud. Surf. Sci. Catal.* **1999**, *127*, 269–277.

33. Barba, D.; Cammarota, F.; Vaiano, V.; Salzano, E.; Palma, V. Experimental and numerical analysis of the oxidative decomposition of H_2S. *Fuel* **2017**, *198*, 68–75. [CrossRef]
34. Jüngst, E.; Nehb, W. Hydrogen sulfide to sulfur (Claus process). In *Handbook of Heterogeneous Catalysis*; Wiley-VCH: Weinheim, Germany, 2008; pp. 2609–2623.
35. Huang, W.-F.; Chen, H.-T.; Lin, M.C. Density functional theory study of the adsorption and reaction of H_2S on TiO_2 rutile (110) and anatase (101) surfaces. *J. Phys. Chem. C* **2009**, *113*, 20411–20420. [CrossRef]
36. Arrouvel, C.; Toulhoat, H.; Breysse, M.; Raybaud, P. Effects of P_{H2O}, P_{H2S}, P_{H2} on the surface properties of anatase-TiO_2 and g-Al_2O_3: A DFT study. *J. Catal.* **2004**, *226*, 260–272. [CrossRef]
37. Fahmi, A.; Ahdjoudj, J.; Minot, C. A theoretical study of H_2S and MeSH adsorption on TiO_2. *Surf. Sci.* **1996**, *352–354*, 529–533. [CrossRef]
38. Markovits, A.; Ahdjoudj, J.; Minot, C. Theoretical study of the TiO_2 and MgO surface acidity and the adsorption of acids and bases. *Mol. Eng.* **1997**, *7*, 245–261. [CrossRef]
39. Abbasi, A.; Sardroodi, J.J. Adsorption and dissociation of H_2S on nitrogen-doped TiO_2 anatase nanoparticles: Insights from DFT computations. *Surf. Interface* **2017**, *8*, 15–27. [CrossRef]
40. Ma, H.L.; Yang, J.Y.; Dai, Y.; Zhang, Y.B.; Lu, B.; Ma, G.H. Raman study of phase transformation of TiO_2 rutile single crystal irradiated by infrared femtosecond laser. *Appl. Surf. Sci.* **2007**, *253*, 7497–7500. [CrossRef]
41. Mino, L.; Spoto, G.; Bordiga, S.; Zecchina, A. Particles morphology and surface properties as investigated by HRTEM, FTIR, and periodic DFT calculations: From pyrogenic TiO_2 (P25) to nanoanatase. *J. Phys. Chem. C* **2012**, *116*, 17008–17018. [CrossRef]
42. Martra, G. Lewis acid and base sites at the surface of microcrystalline TiO_2 anatase: Relationships between surface morphology and chemical behaviour. *Appl. Catal. A* **2000**, *200*, 275–285. [CrossRef]
43. Spoto, G.; Morterra, C.; Marchese, L.; Orio, L.; Zecchina, A. The morphology of TiO_2 microcrystals and their adsorptive properties towards CO: A HRTEM and FTIR study. *Vacuum* **1990**, *41*, 37–39. [CrossRef]
44. Signorile, M.; Damin, A.; Budnyk, A.; Lamberti, C.; Puig-Molina, A.; Beato, P.; Bordiga, S. MoS_2 supported on P25 titania: A model system for the activation of a HDS catalyst. *J. Catal.* **2015**, *328*, 225–235. [CrossRef]
45. Cesano, F.; Bertarione, S.; Uddin, M.J.; Agostini, G.; Scarano, D.; Zecchina, A. Designing TiO_2 based nanostructures by control of surface morphology of pure and silver loaded titanate nanotubes. *J. Phys. Chem. C* **2010**, *114*, 169–178. [CrossRef]
46. Bordiga, S.; Scarano, D.; Spoto, G.; Zecchina, A.; Lamberti, C.; Otero Areán, C. Infrared study of carbon monoxide adsorption at 77 K on faujasites and ZSM-5 zeolites. *Vib. Spectrosc.* **1993**, *5*, 69–74. [CrossRef]
47. Mino, L.; Ferrari, A.M.; Lacivita, V.; Spoto, G.; Bordiga, S.; Zecchina, A. CO adsorption on anatase nanocrystals: A combined experimental and periodic DFT study. *J. Phys. Chem. C* **2011**, *115*, 7694–7700. [CrossRef]
48. Davydov, A.; Chuang, K.T.; Sanger, A.R. Mechanism of H_2S oxidation by ferric oxide and hydroxide surfaces. *J. Phys. Chem. B* **1998**, *102*, 4745–4752. [CrossRef]
49. Murphy, A.B. Band-gap determination from diffuse reflectance measurements of semiconductor films, and application to photoelectrochemical water-splitting. *Sol. Energy Mater. Sol. Cells* **2007**, *91*, 1326–1337. [CrossRef]
50. Li, N.; Zhang, X.; Zhou, W.; Liu, Z.; Xie, G.; Wang, Y.; Du, Y. High quality sulfur -doped titanium dioxide nanocatalysts with visible light photocatalytic activity from non-hydrolytic thermolysis synthesis. *Inorg. Chem. Front.* **2014**, *1*, 521–525. [CrossRef]
51. Ho, W.; Yu, J.C.; Lee, S. Low-temperature hydrothermal synthesis of S-doped TiO_2 with visible light photocatalytic activity. *J. Solid State Chem.* **2006**, *179*, 1171–1176. [CrossRef]
52. Chen, X.; Burda, C. The electronic origin of the visible-light absorption properties of C-, N- and S-doped TiO_2 nanomaterials. *J. Am. Chem. Soc.* **2008**, *130*, 5018–5019. [CrossRef] [PubMed]
53. Tang, X.; Li, D. Sulfur-doped hhighly ordered TiO_2 nanotubular arrays with visible light response. *J. Phys. Chem. C* **2008**, *112*, 5405–5409. [CrossRef]
54. Umebayashi, T.; Yamaki, T.; Itoh, H.; Asai, K. Band gap narrowing of titanium dioxide by sulfur doping. *Appl. Phys. Lett.* **2002**, *81*, 454–456. [CrossRef]

Supplementary Materials: Article Sulfur-doped TiO_2: structure and surface properties

Sara Cravanzola*, Federico Cesano*, Fulvio Gaziano and Domenica Scarano

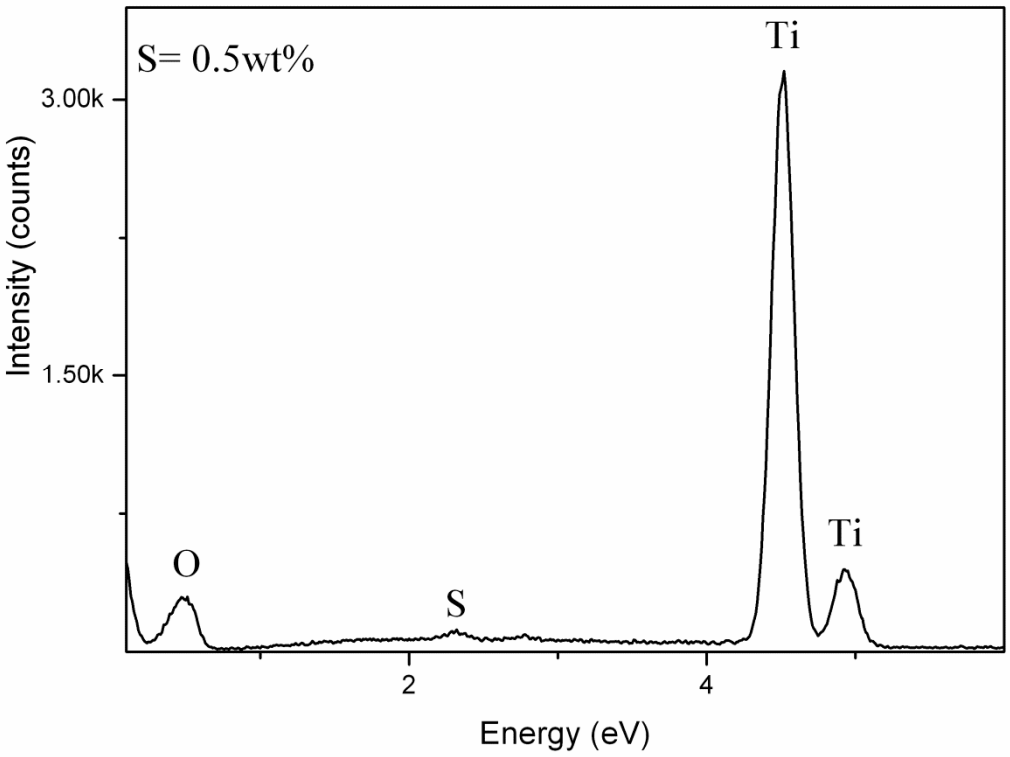

Figure S1. EDAX spectrum of TiO2/H2S.

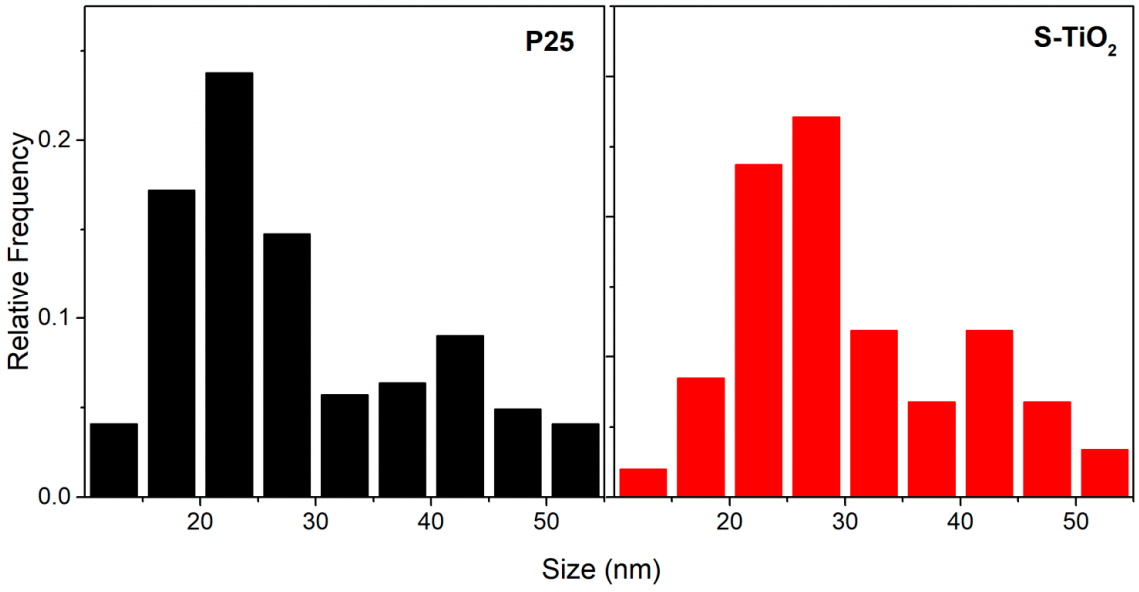

Figure S2. Particle size distributions (PSDs) of TiO_2 P25 (left panel) and of S-TiO_2 (right panel).

Table S1. Mean crystal sizes of anatase and rutile nanoparticles in TiO_2 P25 and S-TiO_2 samples, as obtained from XRD peak broadening (black and red patters in Figure 1).

TiO_2 P25	
(101) Anatase	25 nm
(110) Rutile	40 nm
S-TiO2	
(101) Anatase	26 nm
(110) Rutile	41 nm

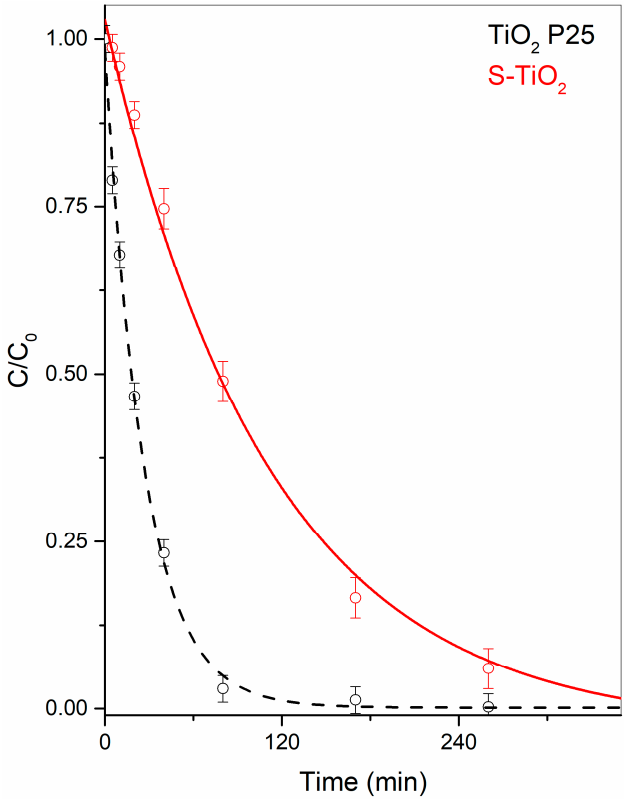

Figure S3. Time dependence of C/C_0 upon solar light exposure of S-TiO_2 (red line) as compared to the TiO_2 P25 (black dotted line), for photodegradation of methylene blue.

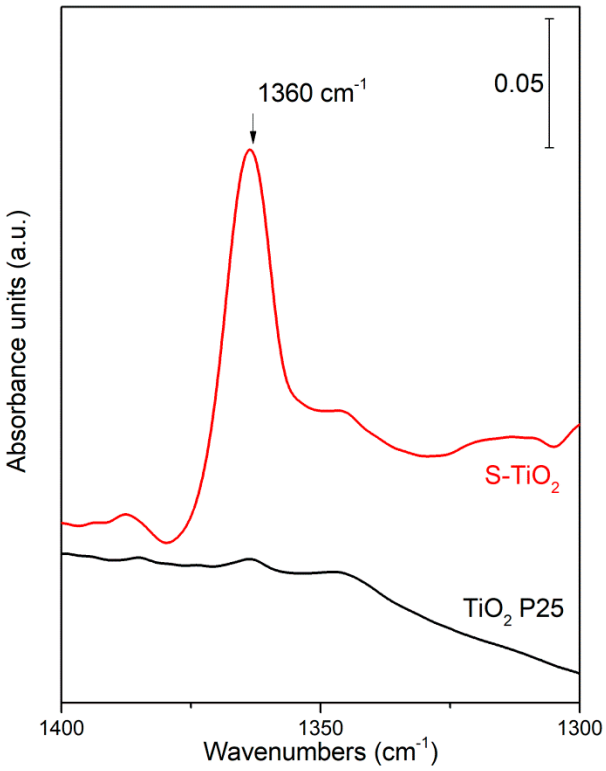

Figure S4. FTIR spectra, recorded before CO dosage, of TiO_2 (black curve) and TiO_2/H_2S (red curve).